CALIBRATION OF TRANSDUCERS FOR ACOUSTIC EMISSION

Petr Hora

An impulse method for calibration of transducers for acoustic emissions is presented. The calibrating device and standard conic- and cylindrical transducers are described in detail. Attention is paid also to calculating displacements on the surface of a half-space, since the calculation cannot be avoided. For calculation of displacements in epicentrum and in its close neighbourhood by subsurface vibration excitation, aproximation functions have been determined. These functions approximate an exact solution with errors less than 1%, and accelerate calculations considerably.

LIST OF SYMBOLS

a	radius
a_1, a_2	radii of cone waveguide
c	phase velocity
c_R	velocity of Rayleigh's waves
c_0	velocity of a longitudinal wave in a thin rod
c_1	velocity of a dilatation wave in an unlimited three-dimensional medium
c_2	velocity of a transversal wave
g_{33}	piezoelectric constant
h_{33}	piezoelectric constant
k	wave number
k_b	transformation ratio
l	length
r	radius, ratio of radii of a cone waveguide
s_{33}^D	yielding constant at $D = 0$
t	time
v	velocity
x_1, x_2	parameters of a cone waveguide
C_0	transducer capacity
$F(t)$	exciting force
S_1, S_2	areas of bases of a cone waveguide
U	electric voltage

γ	velocity ratio c_2/c_R
δ	velocity ratio c_1/c_2
λ	Lamé's constant, wavelength
μ	Lamé's constant
ξ	displacement
ϱ	density
σ	Poisson's ratio
τ	time, dimensionless time
ω	angular frequency
Δ	relative deviation
$1(t)$	Heaviside's step function

1. INTRODUCTION

The following calibration methods are used at present:

vibration method

is used especially for calibration of accelerometers. On a vibrating table there is placed both the transducer to be tested and the standard transducer. The vibrating table excited by a sine generator may cover a frequency range from 1 Hz to 100 kHz, the practical upper limit being approximately 20 kHz (the frequency limitation is due to mechanical resonances of the vibrating table). An output signal of the transducer being calibrated is compared with the output signal of the standard transducer subjected to the same load. The sensitivity is given directly in pC/g or in mV/g.

impulse method

makes use of a stress wave excited by breaking either a glass capillary or graphite, and/or through an impact of a small ball falling from a defined height upon the surface of a trial medium on which is situated both the transducer being tested and the standard transducer. This method, which affords an absolute calibration, will be described in detail in this paper.

hydrophone method

The calibration is carried out in a great water tank on whose opposite sides are situated a standard transmitter and a standard transducer. On measuring the transmission throughout the full frequency band, the standard transducer is replaced by the transducer being tested. The calibrating curve is obtained by comparing the two measurements. This method necessitates preserving equivalent geometry. The usual frequency range is from 1 kHz to 1 MHz.

ultrasound method

is a modification of the preceding method. Here, the transmitter is directly acoustically connected with the transducer through the agency of a viscous medium. The

ultrasound method

random noise method

aims at simulating the signal of acoustic emission, including the conditions for its propagation and sensing. The transducer is situated on the surface of a capacious block of material excited by a flux of fine hard particles. The impact of the particles generates stress waves which propagate through the material and enter the transducer. The signal is of a noise nature with a wide frequency spectrum. The ouptut from the transducer is connected to a frequency analyser. The dependence of amplitude on frequency is then recorded in a suitable way. This method of generating impulses is in a good agreement with real relations by acoustic emission. An individual impact of a particle can well imitate a point source of a narrow transient impulse. The nature of these continuous impacts is then quite random.

spark calibration method

is a modification of the preceding method. Here, short stress impulses are generated by a pressure wave aroused by a discharge in an air spark gap. On the assumption that surface waves entering the transducer contain all frequency components with equal amplitudes, we can insert a narrow-band filter on the output from the transducer and thus measure amplitudes of these components, to obtain the frequency characteristic of the transducer.

It is seen that the suitableness of the above methods for calibrating transducers of acoustic emissions is specialized. Accelerometers and conventional ultrasound exciters and transducers are at present calibrated through proved methods. However, these methods are not in correlation with real acoustic emission.

On comparing theoretical and practical results and respecting the regions of applicability, the calibration procedure must satisfy the following requirements:

a) An input calibration signal must have the form of stress impulses with a small amplitude and a short period of existence.

b) The propagation of impulses in a calibration device must be similar to propagation of signals of acoustic emission.

c) Bond conditions of a transducer in the respective device must approximate to real conditions in practical applications.

d) Calibration tests must yield reproducible results, and they must be exact with an adequate and permanent tolerance.

With reference to the above requirements it is evident that optimum results by calibrating transducers for acoustic emission may be at present achieved via the impulse method.

2. IMPULSE METHOD OF CALIBRATION

The principle of the impulse method consists in comparing signals obtained from a standard reference transducer and the transducer being calibrated. The two signals are subjected to FFT, divided by each other, and the result is multiplied by the frequency characteristic of the reference transducer. Thus we get the frequency characteristic of the transducer being calibrated. Signals from the transducers correspond to stress waves which are excited by breaking either a glass capillary or graphite, and/or by an impact of a small ball upon the surface of a trial medium. The trial medium is usually represented by a steel cylinder with as great radial and axial dimensions as possible. In this way we may ensure a sufficiently long time interval for an undisturbed record (i.e. without rebounds) of stress waves.

The transducers and the exciting source may be situated either on one base of the cylinder (surface excitation) or on opposite bases (subsurface excitation) (Fig. 1).

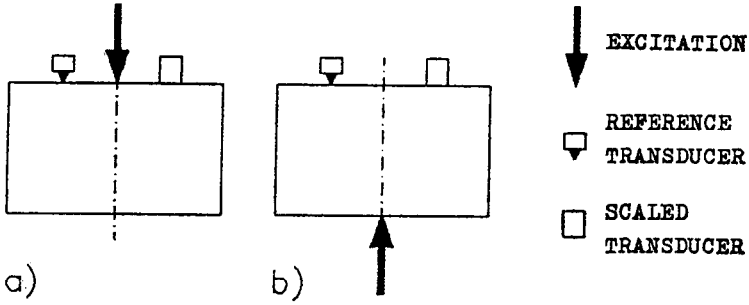

Fig. 1. Scheme of calibration for a) surface- and b) subsurface excitation.

The latter method doesn't suffer from the aperture phenomenon, however, in this case, the intensity level is one order of magnitude smaller, which results in worse noise relations.

As the standard transducer we usually use a capacity transducer or a transducer with a conic piezoceramic. These transducers are very sensitive, and they are distinguished by an even characteristic over a wide frequency range (from tens of kHz to units of MHz). A detailed description of the conic transducer is given in paragraph 4.

Since the calculation of frequency characteristic of the transducer being calibrated necessitates the knowledge of the reference transducer characteristic, we will show the measuring method for the reference conic transducer.

The method of calibrating the standard transducer consists in calculating time dependences of an axial component of displacement vector on the surface of a half space by both surface- and subsurface excitation through a step function of force. Then, by exciting the half-space (represented by a spacious steel cylinder) through

a step force we can compare the signal from a conic transducer with theoretical values, to obtain the frequency characteristic of the reference conic transducer. Again, we can use either a surface- or subsurface excitation (Fig. 2). The results of the calibration are presented in paragraph 6.

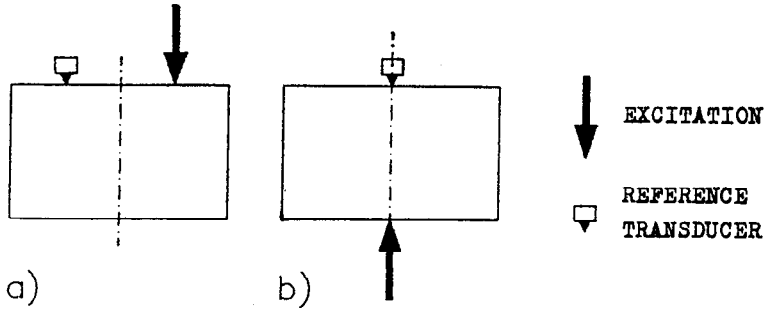

Fig. 2. Scheme of calibration of a reference transducer for a) surface- and b) subsurface excitation.

3. DISPLACEMENTS ON SURFACE OF HALF-SPACE

As mentioned above, the calibration of a standard transducer necessitates calculating time dependences of an axial component of displacement vector on the surface of a half-space by both surface- and subsurface excitation through a step function of force. Below, therefore, we will give the results of these calculations.

3.1. The case of surface excitation through a step function of force

The situation is illustrated in Fig. 3. The time dependence of an axial component of the vector of displacement l_z on the surface of a half-space ($z = 0$) is shown in Fig. 4, notably, the scaled axial component of the vector of displacement $L_z(\tau)$ versus

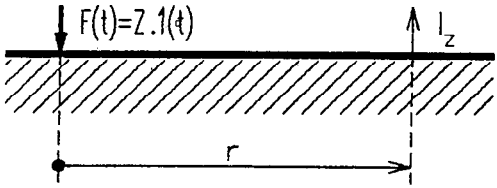

Fig. 3. The case of surface excitation of half-space.

dimensionless time τ is plotted, where

$$\tau = (c_2/r)\, t$$

and

$$L_z(\tau) = \frac{l_z(\tau)}{\left[\dfrac{\delta^2 Z}{\pi^2 \mu r}\right]}.$$

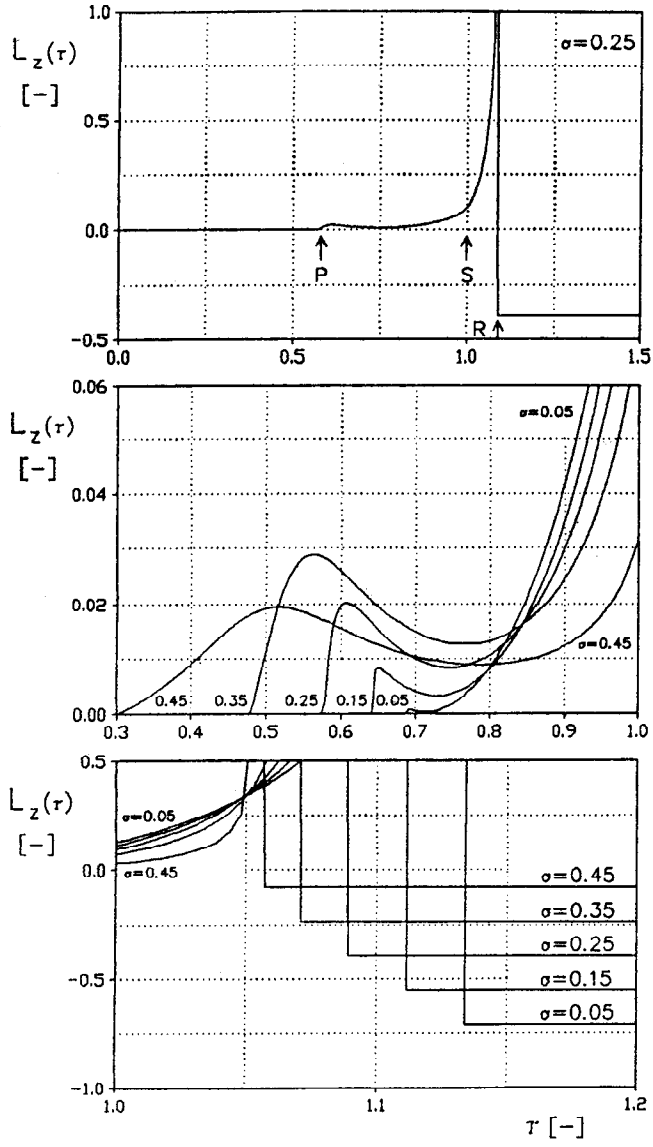

Fig. 4. Time dependence of a scaled axial component of displacement.

For the calculation we used the Pekeris solution in the closed form [8], which was adjusted for numeric calculation by Mooney [7].

It is to be remarked to Fig. 4 that:

– all responses are directly proportional to the total force Z,

– the succession of arrivals of the respective waves is as follows:

i) longitudinal wave (P), ii) transversal wave (S), and iii) Rayleigh's wave (R),

– for $\tau < 1/\delta$ the value of $L_z(\tau)$ is zero, since the longitudinal wave propagating at highest velocity could not arrive at the place considered,

– with increasing the value of Poisson's ratio there increases the length of the interval between arrival of longitudinal ($\tau = 1/\delta$) and transversal ($\tau = 1$) wave, whereas the interval between arrival of transversal ($\tau = 1$) and Rayleigh's ($\tau = \gamma$) wave decreases. This is due to the well-known dependence of velocities c_1, c_2 and c_R on Poisson's ratio,

– with increasing Poisson's ratio there increases the amplitude of the pulse at the instant of arrival of a longitudinal wave (only for $\sigma < 0{\cdot}35$) and length of this pulse, whereas the steepness of the pulse decreases. The effect of decreasing the steepness would be more pronounced in a real- than in dimensionless time,

– the arrival of a transversal wave ($\tau = 1$) is represented only by the change in the steepness of the response (step in derivative). This change in the steepness is more pronounced at higher values of Poisson's ratio (below, we will show that the change in the steepness of responses obtained experimentally can be only hardly identified),

– with increasing Poisson's ratio the width of Rayleigh's pulse becomes considerably smaller,

– the constant level of $L_z(\tau)$, which follows after Rayleigh's pulse, decreases if the value of Poisson's ratio grows,

– all curves are running through a common point $\tau = 1{\cdot}05$. From the physical angle this point is the point of arrival of Rayleigh's wave in the limit case of an ideal fluid.

3.2. The case of subsurface excitation through a step function of force

The situation is illustrated in Fig. 5. The time dependence of an axial component of the vector of displacement l_z on the surface of a half-space ($z = 0$) is shown in Fig. 6, notably, the scaled axial component of the vector of displacement $L_z(\tau)$ versus dimensionless time τ is plotted for various values of ratio r/h at $\sigma = 0{\cdot}25$,

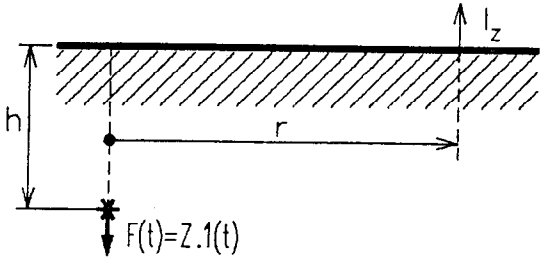

Fig. 5. The case of subsurface excitation of half-space.

where

$$\tau = (c_2/R)\, t\,,$$

$$L_z(\tau) = \frac{l_z(\tau)}{\left[\frac{\delta^2 Z}{\pi^2 \mu R}\right]}$$

and

$$R = \sqrt{(r^2 + h^2)}\,.$$

The calculation was carried out via the Pekeris solution in the closed form[9, 10]. This solution holds for a half-space characterized by elastic constants λ and μ. The constants are supposed to be identical ($\lambda = \mu \Rightarrow \delta = 3$; hence, Poisson's body is in question).

It is to be remarked to Fig. 6 that:

- P-wave starts with a finite displacement whose direction is the same as that of the force in the source. If the force in a subsurface source is oriented upwards, the initial displacements of P-wave would be directed upwards too. It should be remarked that with decreasing the depth of the source h (or with increasing r) the initial displacement of P-wave inclines to zero.
- the character of S-wave is in the case $r < h/\sqrt{2}$ quite different from the case when $r > h/\sqrt{2}$. In the former case the arrival of S-wave is distinguished by a finite step in the displacement, whereas in the latter case the S-wave is distinguished by an infinite step in the displacement which is oriented oppositely than in the former case. It is evident that if $r < h/\sqrt{2}$ the arrival of S-wave is distinguished by discontinuity of the displacement directed downwards. At the arrival of S-wave the step in the vertical component is directed in the same direction as in the case of P-wave. If $r > h/\sqrt{2}$ the S-wave is distinguished by an infinite step in the displacement which is oriented oppositely than in the case $r < h/\sqrt{2}$. An infinite step doesn't occur in the case of a surface pulse ($h = 0$), as can be seen from Fig. 4.
- at the instant of arrival of SP-wave its amplitude is zero, which contrasts with discontinuities occurring by arrivals of P- or S-wave. This weak start may be referred to the fact that in terms of the ray theory [1] the SP-wave transports no energy at its arrival. Accordingly, there appears only a cut occurring after arrival of the SP-wave. The displacement following the arrival of SP-wave is directed upwards. It should be remarked that the evident convergence of P- and SP-period occuring at great distances in Fig. 6 is due to the existence of a dimensionless time scale which is used on the axis of the independent variable. If an absolute time scale is used, and if great distances are in question, the time delay of SP-wave behind P-wave approximates to the limit value

  $$(h/c_2)\sqrt{2/3}$$

- Rayleigh's wave doesn't exist in the range $r < h/\sqrt{2}$. At $r = 5h$ Rayleigh's wave starts appearing, while at $r = 10h$ it can be clearly seen. At $h = 0$ the case is

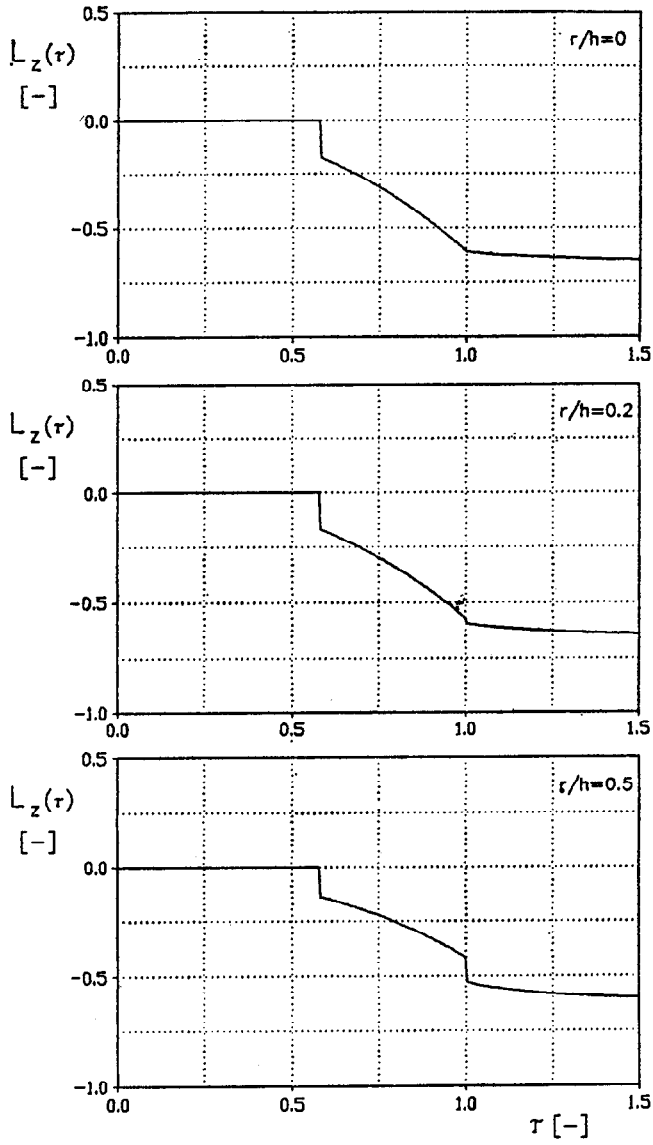

identical with that described in the preceding paragraph (see Fig. 4). The amplitude of Rayleigh's waves in Fig. 6 increases with increasing the distance. This is due to the fact that for scaling the factor $1/R$ is used, while the surface waves are dying away with $1/\sqrt{R}$. Really, we can find out that amplitudes of maximum values of L_z, which occur at the arrival of Rayleigh's wave, become, with increasing the distance, greater as $\sqrt{R}$. The curves shown in Fig. 6, which indicate the change in character of displacements, occurring if r/h increases, may be also considered

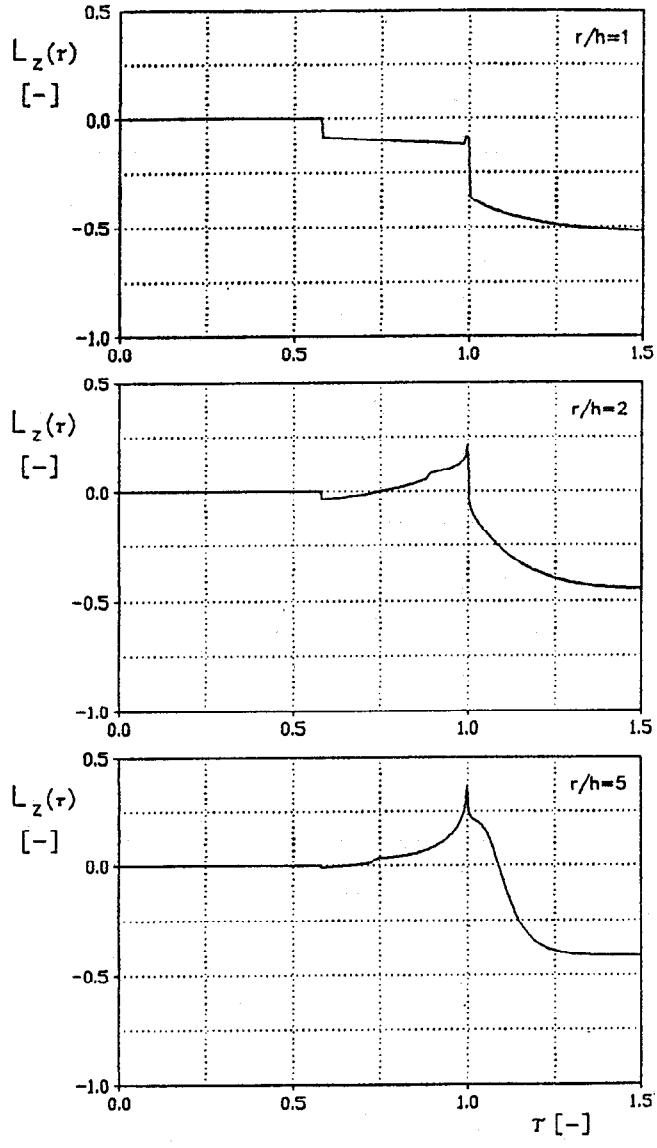

to illustrate the effect of decreasing depth h at constant value of r. If the source moves towards the surface, there appear high-frequency components of Rayleigh's waves with relatively greater amplitudes. As a result of using the scaled time τ instead of absolute time t, the increase in amplitudes is somewhat blown up in Fig. 6.

– since the loading force follows Heaviside's unit function, we get for $t \to \infty$ a finite displacement.

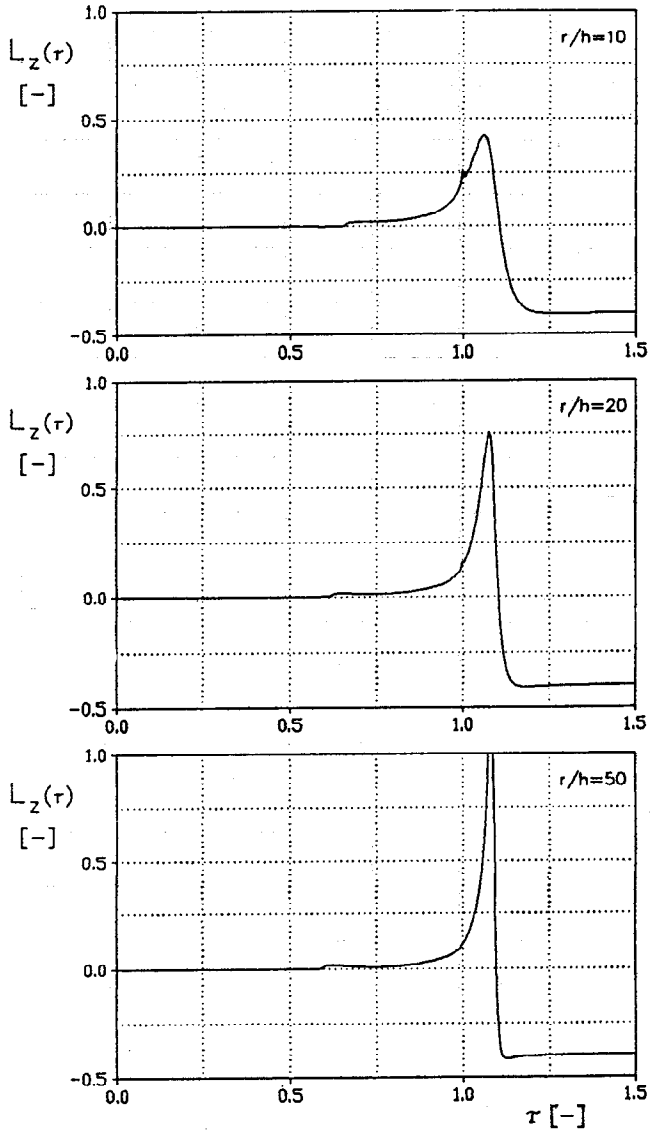

Fig. 6. Time dependence of scaled axial component of displacement.

3.3. Approximation of solution for $r < h/\sqrt{2}$

The calculation by [9, 10] is much time consuming. Accordingly, we tried to find a suitable approximation of relations for $L_z(\tau)$. This approximation was supposed only for solutions at $r < h/\sqrt{2}$, since this interval covers the range of practical applications, where the case $r = 0$ (measuring in epicentrum) occurs in the majority of cases.

A typical curve of $L_z(\tau)$ at $r < h/\sqrt{2}$ is shown in Fig. 7. The approximation was divided into two steps. First, we approximated a part of the response in a dimensionless time interval $\langle 1/\sqrt{3}; 1)$. For this interval the function ${}_I L_z^*(\tau)$ was approximated in the form

$$ {}_I L_z^*(\tau) = -Ae^{\alpha\tau} - L, $$

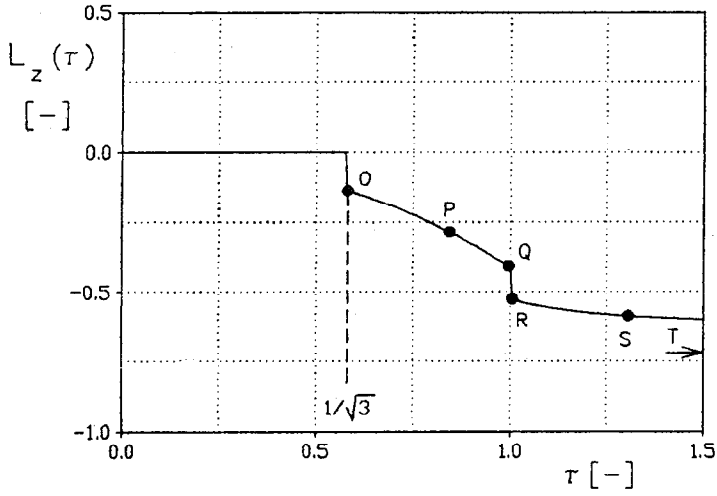

Fig. 7. Typical course $L_z(\tau)$ for $r < h/\sqrt{2}$.

where A, α, and L are real numbers, and $A, \alpha > 0$. To obtain constants A, α and L, we must find three equations for these three constants, which represent the passage of approximating function ${}_I L_z^*(\tau)$ through three important points:

a) point O $[1/\sqrt{3};\ L_z(1/\sqrt{3})]$,
b) point P $[\tau';\ L_z(\tau')]$ (the selection of τ' – see below),
c) point Q $[1;\ L_z(1_-)]$,

$$ \begin{aligned} L_z(1/\sqrt{3}) &= -Ae^{\alpha/\sqrt{3}} - L \\ L_z(\tau') &= -Ae^{\alpha\tau'} - L \\ L_z(1_-) &= -Ae^{\alpha} - L \end{aligned} \qquad (1) $$

On subtracting the third equation from the first one, and the second equation from the first one, we get the system of equations

$$ \begin{aligned} L_z(1/\sqrt{3}) - L_z(1_-) &= -A(e^{\alpha/\sqrt{3}} - e^{\alpha}) \\ L_z(1/\sqrt{3}) - L_z(\tau') &= -A(e^{\alpha/\sqrt{3}} - e^{\alpha\tau'}) \end{aligned} \qquad (2) $$

On dividing these equations, we have

$$ \frac{L_z(1/\sqrt{3}) - L_z(1_-)}{L_z(1/\sqrt{3}) - L_z(\tau')} = \frac{e^{\alpha/\sqrt{3}} - e^{\alpha\tau'}}{e^{\alpha/\sqrt{3}} - e^{\alpha\tau'}} \qquad (3) $$

which allows the constantnt α to be calculated. Equation (3) is transcendental, and it was solved via bisection (i.e., step halving method). Substituting α into equation (2), we get constant A, and on substituting α and A into (1), we get constant L.

Now, let us return to the selection of τ'. For τ' we can successively substitute the values from interval $\langle 1/\sqrt{3}; 1)$. For all values of τ' we will calculate constants A, α, L and maximum deviation $|L_z(\tau) - {}_I L_z^*(\tau)|$ in the given interval $\langle 1/\sqrt{3}; 1)$. On selecting minimum values of these maximum deviations, we will regard as finite values of constants A, α, L those values corresponding to this minimum maximum of deviations of the approximated- and approximating function.

The values of constants A, α, L and the values of relative devations for various values of r/h are listed in Tab. 1.

Table 1. Constants A, α, L in dependence on r/h.

r/h	A	α	L	Δ [%]
0·0	0·1530111	1·7108337	−0·2363360	0·683
0·1	0·1492081	1·7156433	−0·2291425	0·674
0 2	0·1384420	1·7267851	−0·2086799	0·260
0·3	0·1228694	1·7497802	−0·1786599	0·602
0·4	0·1039841	1·7779663	−0·1418856	0·520
0·5	0 0846565	1·8071838	−0·1034586	0·407
0·6	0·0663195	1·8345214	−0·0661979	0·243
0·7	0·0500353	1·8529602	−0·0322745	0·054

Now, we will approximate the response within the dimensionless time interval $\langle 1; \infty)$. Here, the approximating function ${}_{II}L_z^*(\tau)$ is assumed in the form

$$ {}_{II}L_z^*(\tau) = Be^{-\beta\tau} - K\,,$$

where B, β, and K are real numbers, and B, $\beta > 0$.

To obtain constants B, β and K, we must again find three equations representing the passage of approximating function ${}_{II}L_z^*(\tau)$ through three important points:

a) point R $[1; L_z(1_+)]$,
b) point S $[\tau'; L_z(\tau')]$, (the selection of τ' − see below)
c) point T $[\infty; L_z(\infty)]$,

$$\begin{aligned} L_z(1_+) &= Be^{-\beta} - K \\ L_z(\tau) &= Be^{-\beta\tau'} - K \\ L_z(\infty) &= Be^{-\beta\infty} - K = -K \end{aligned} \qquad (4)$$

The third equation yields the value of constant K. On dividing the first and second equation, we get the relation

$$\frac{L_z(1_+) + K}{L_z(\tau') + K} = e^{-\beta(1-\tau')} \qquad (5)$$

which allows constant β to be calculated

$$\beta = \frac{1}{\tau' - 1} \ln \frac{L_z(1_+) + K}{L_z(\tau') + K} .$$

On substituting constant β into equation (4), we get constant B.

The selection of τ' is analogous to that carried out in the preceding part. We will successively substitute for τ' the values from interval $\langle 1; 1{\cdot}5\rangle$ whose upper limit was chosen with reference to practical measurements which do not allow to go far beyond the value $\tau = 1$ (for greater values there appear rebounds from the walls of the trial block). For all values τ' we will calculate constants B, β, K and maximum deviation $|L_z(\tau) - {}_{II}L_z^*(\tau)|$ in the given interval $\langle 1; 1{\cdot}5\rangle$. On selecting the minimum of these maximum deviations, we will regard as finite values of constants B, β, K those values corresponding to this minimum maximum of deviations of the approximated and approximating function.

The values of constants B, β, K and the values of relative deviations for various values of r/h are listed in Tab. 2. From Tab. 1 and Tab. 2 it is seen that constants

Table 2. Constants B, β, K in dependence on r/h.

r/h	B	β	K	Δ [%]
0·0	5·4178353	4·8089727	0·6544984	0·206
0·1	5·7000910	4·8305700	0·6519063	0·207
0·2	6·5926408	4·8926104	0·6444292	0·204
0·3	8·4223636	5·0100552	0·6328820	0·201
0·4	11·8377902	5·1900530	0·6183882	0·197
0·5	21·8775353	5·6168730	0·6021385	0·340
0·6	85·692129	6·7567409	0·5851986	1·027
0·7	10726·9568449	11·2532219	0·5684033	3·953

$A, \alpha, L, B, \beta, K$ are monotonous functions of ratio r/h. This fact allows us to find simple approximations also for these functions. The approximation was carried out via the least squares method, the approximating function being represented by the polynoms

$$P(x) = \sum_{i=0}^{n} a_i x^i , \quad \text{where} \quad x = r/h .$$

To approximate A, α, L, K, we used the polynoms of the third degree, while for B and β respectively the polynoms of the eighth and seventh degree have been used since the values B and β grow very rapidly with increasing ratio r/h. The values of coefficients of the polynoms which approximate dependences A, α, K and B, β, K on r/h are listed in Tab. 3 and Tab. 4.

Table 3. Coeficients of polynoms approximating dependences of A, α, L on r/h.

coefficient	A	α	L
a_0	0·153071466	1·711730686	−0·236399646
a_1	0·000886007	−0·056858945	−0·004390876
a_2	−0·435356166	0·806968492	0·834623952
a_3	0·320118097	−0·623369925	−0·588797609

Table 4. Coefficients of polynoms approximating dependence of B, β, K on r/h.

coefficient	B	β	K
a_0	5·41521852e0	4·80896930e0	0·654486469
a_1	8·61037755e3	3·27977117e0	0·003364517
a_2	−2·02161622e5	−7·57690498e1	−0·304874194
a_3	1·72750784e6	6·89884028e2	−0·177750512
a_4	−6·81450118e6	−2·99445366e3	
a_5	1·19872070e7	6·84589597e3	
a_6	−3·81155786e6	−7·93593483e3	
a_7	−1·36377332e7	3·72389071e3	
a_8	1·22162426e7		

Table 5. Maximum relative deviations.

r/h	Δ_{I} [%]	Δ_{II} [%]
0·0	0·855	0·189
0·1	0·308	0·149
0·2	0·340	0·246
0·3	0·656	1·392
0·4	0·789	3·604
0·5	0·419	7·297
0·6	0·216	12·643
0·7	0·312	18·994

Tab. 5 presents maximum relative deviations for individual values r/h, which have been obtained comparing real responses $L_z(\tau)$ with approximating responses ${}_{I}L_z^*(\tau)$ and ${}_{II}L_z^*(\tau)$.

4. CONIC TRANSDUCERS

A conic transducer is a highly sensitive wide-band device (operating up to several MHz) for measuring a vertical component of displacement of a small area on the surface of a body. This transducer is designed for a wide region of applications, e.g., for testing by means of acoustic emission, to be used as a standard transducer, and the like. The scheme of a conic transducer is shown in Fig. 8.

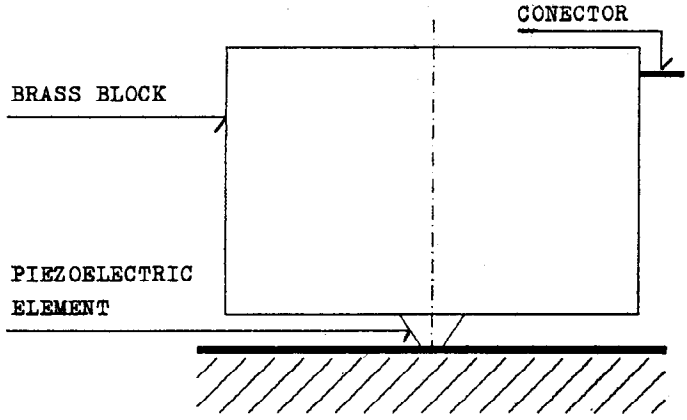

Fig. 8. Scheme of a conic transducer.

The basic characteristics of the transducer are as follows:

1) Active element made of piezoceramics is conic, its polarization is parallel with the axis of the cone;

2) The greater base of the cone with scalded silver or gold electrode is sticked (or soldered) on a relatively great cylindrical block made usually from brass;

3) The smaller base of the cone with scalded silver or gold electrode is connected through the medium of as thin binding layer as possible with the part of relatively large surface on which is measured the vertical component of displacement;

4) No-load voltage is measured between the brass cylindrical block and the surface.

Now we are going to determine an equivalent diagram of the conic transducer, and to calculate its frequency characteristic from geometrical dimensions and material constants of an active element and terminal impedances.

By designing an equivalent diagram we will use as a basis an impedance matrix of a conic divergent waveguide (see Fig. 9) in solid phase [6, 11]

$$Z_m = \begin{bmatrix} \varrho c S_1 \left(\frac{\operatorname{cotg}(kl)}{j} + \frac{1}{jkx_1} \right) ; & -\varrho c \sqrt{(S_1 S_2)} \frac{1}{j \sin(kl)} \\ \varrho c \sqrt{(S_1 S_2)} \frac{1}{j \sin(kl)} ; & -\varrho c S_2 \left(\frac{\operatorname{cotg}(kl)}{j} - \frac{1}{jkx_2} \right) \end{bmatrix}.$$

This impedance matrix was derived on the assumption that the sections perpendicular to the axis of waveguide remain by deformation planar, the axial stress is uniformly distributed all over the surface, and radial displacements can be neglected. Comparing

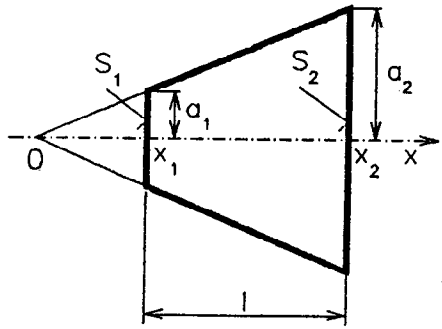

Fig. 9. Conic divergent waveguide.

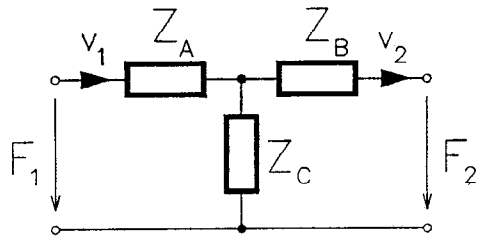

Fig. 10. T-element.

the above relation with the matrix of *T*-element shown in Fig. 10,

$$Z_T = \begin{bmatrix} Z_A + Z_C; & -Z_C \\ Z_C; & -Z_B - Z_C \end{bmatrix}$$

we get for Z_A, Z_B and Z_C the following relations

$$Z_A = \varrho c S_1 \left[\frac{\operatorname{cotg}(kl)}{j} + \frac{1}{j\, kx_1} - \frac{r}{j \sin(kl)} \right], \tag{6}$$

$$Z_B = \varrho c S_2 \left[\frac{\operatorname{cotg}(kl)}{j} - \frac{1}{j\, kx_2} - \frac{1/r}{j \sin(kl)} \right], \tag{7}$$

$$Z_C = \varrho c \sqrt{(S_1 S_2)} \frac{1}{j \sin(kl)} \quad , \tag{8}$$

where $r = x_2/x_1$.

If the *T*-element is supplemented by Mason's model, we get an equivalent diagram of an peizoelectric element whose shape is conic (see Fig. 11).

Transferring the electric part to the mechanical side and on supplementing the

diagram by source impedance Z_1 and load impedance Z_2 (see Norton's theorem – velocity short-circuited + parallel impedance Z_1), we get an equivalent diagram of a conic transducer, indicated in Fig. 12. It should be remarked that v, v_1 and v_2

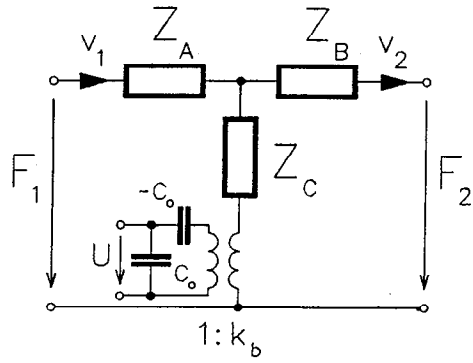

Fig 11. Equivalent diagram of a conic piezoelectric element.

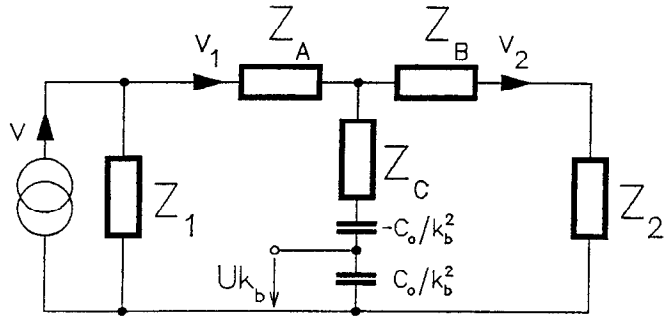

Fig. 12. Equivalent diagram of conic transducer.

are loop velocities (not branch velocities), for instance, the velocity on Z_C is $v_1 - v_2$.

For the diagram shown in Fig. 12 it holds

$$v_1 - v_2 = vF\,, \tag{9}$$

where

$$F = \frac{Z_1(Z_B + Z_2)}{(Z_A + Z_1 + Z_C)(Z_B + Z_2 + Z_C) - Z_C^2} \tag{10}$$

and

$$Uk_B = \frac{v_1 - v_2}{j\omega C_0/k_b^2}. \tag{11}$$

On substituting for v_1-v_2 from eguation (9) into eguation (11), we obtain

$$Uk_b = \frac{v}{j\omega}\frac{k_b^2}{C_0}F\,.$$

Further, substituting $\xi = v/j\omega$ and $-p_{33} = k_b/c_0$, we get

$$U/\xi = -p_{33}F\,,$$

which is the resultant relation for sensitivity of a conic transducer.

The value of p_{33} lies between h_{33} (disc) and g_{33}/s_{33}^D (rod).
h_{33} is piezoelectric constant (for calculation we used the value $21{\cdot}5 \,.\, 10^8$ V/m).
g_{33} is piezoelectric constant (for calculation we used the value $24{\cdot}9 \,.\, 10^{-3}$ Vm/N), and
s_{33}^D is the yielding constant at $D = 0$ (for calculation we used the value $9{\cdot}46 \,.\, 10^{-12}$ m^2/N).

Substituting relations (6) and (8) into relation (10) for individual impedances, we get the numerator of fraction F (see (10))

$$N = z_1\left[z_2 + i\left(\frac{1}{r\sin(kl)} + \frac{r-1}{rkl} - \operatorname{cotg}(kl)\right)\right] \tag{12}$$

and denominator of fraction F

$$D = 1 + z_1 z_2 + \frac{(r-1)^2}{r(kl)^2} - \frac{(r-1)^2}{rkl}\operatorname{cotg}(kl) +$$

$$+ i\left[z_1\left(\frac{r-1}{rkl} - \operatorname{cotg}(kl)\right) - z_2\left(\frac{r-1}{kl} + \operatorname{cotg}(kl)\right)\right]. \tag{13}$$

Here z_1 and z_2 are scaled specific impedances $Z_1/\varrho c S_1$ and $Z_2/\varrho c S_2$ (the scaling is carried out to ϱc of the cone!).

In the case of the cylindrical transducer, $r = 1$, we get for F

$$F = \frac{z_1[z_2 + i\,\mathrm{tg}\,(kl/2)]}{1 + z_1 z_2 - i(z_1 + z_2)\operatorname{cotg}(kl)} \tag{14}$$

If kl is equal to odd multiples π, both the numerator and denominator in equation (14) are infinit, but the ratio is finite; if, however, kl is equal to even multiples π, i.e., if length l is equal to integral multiple of wave length, the denominator is infinit for arbitrary values z_1 and z_2, hence, both F and sensitivity U/ξ are nil. In the case of cone, the expression $1/(r\sin(kl))$ for $r > 1$ preserves the finite value of fraction F in equation (12). Instrad of nil, in this case, there exist only minimums in the characteristic. This is the reason why a conic transducer yields a suitably even wide-band characteristic (which cannot be achieved with a cylindrical transducer).

Now it remains to find the values of impedances Z_1 and Z_2. In practical applications the signals detected by a conic transducer are so short that both the body considered and the end block may be supposed to be half-spaces. The problem of the impedance in a half-space, considered in a circular area with radius a on the surface of a half-space, was solved in [2]. Here, the input impedance was approximated by the formula

$$Z = \frac{S\varrho c_1}{g + ib}\,, \tag{15}$$

where

$$g = 1 + 2/x_1(1 - 3y_1/x_1)\frac{\sin(kax_1)}{ka} -$$

$$- 6/x_1^2(1 - 2y_1/x_1)\frac{1 - \cos(kax_1)}{(ka)^2} \tag{16}$$

and

$$b = 2/x_1(2 - 3y_1/x_1)\frac{1}{ka} + 2/x_1(1 - 3y_1/x_1)\frac{\cos(kax_1)}{ka} -$$

$$- 6/x_1^2(1 - 2y_1/x_1)\frac{\sin(kax_1)}{(ka)^2}, \tag{17}$$

where

$$k = \frac{\omega}{c_1}.$$

Here S is the circular area with radius a, and y_1, x_1 are dimensionless parameters obeying equations

$$y_1 = \frac{16}{3\pi}\frac{(1 - \sigma)^2}{(1 - 2\sigma)},$$

$$x_1 = 2\frac{c_1}{c_R} = 2\sqrt{\left(\frac{2(1 - \sigma)}{1 - 2\sigma}\right)}\gamma.$$

The values of γ, x_1, y_1 for various values of Poisson's ratio are listed in Tab. 6.

Fig. 13 illustrates the real and imaginary part of specific impedance $1/(g + ib)$ scaled to ϱc_1, of the material of a half-space (steel).

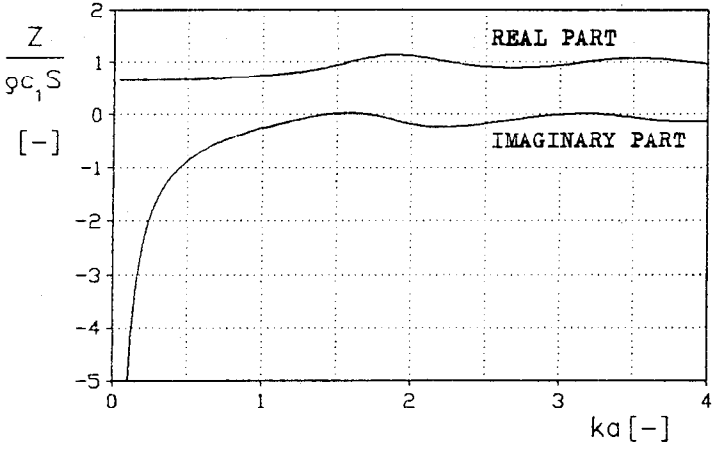

Fig. 13. Dependence of scaled specific impedance $1/(g + ib)$ on ka.

Table 6. Values γ, x_1, y_1 in dependence on σ.

σ	γ	x_1	y_1
0·01	1·14158	3·24530	1·69783
0·03	1·13655	3·26554	1·69928
0·05	1·13161	3·28839	1·70237
0·07	1·12677	3·31415	1·70733
0·09	1·12202	3·34319	1·71442
0·11	1·11738	3·37592	1·72399
0·13	1·11283	3·41284	1·73642
0·15	1·10838	3·45456	1·75222
0·17	1·10403	3·50181	1·77199
0·19	1·09978	3·55549	1·79650
0·21	1·09564	3·61670	1·82673
0·23	1·09160	3·68687	1·86396
0·25	1·08766	3·76778	1·90986
0·27	1·08383	3·86179	1·9666
0·29	1·08010	3·97203	2·03759
0·31	1·07647	4·10278	2·12698
0·33	1·07294	4·26007	2·24140
0·35	1·06950	4·45270	2·39086
0·37	1·06617	4·69413	2·59153
0·39	1·06293	5·00616	2·87135
0·41	1·05878	1·05979	3·28307
0·43	1·05674	6·03098	3·93977
0·45	1·05379	6·99002	5·13540
0·47	1·05092	8·83438	7·94784
0·49	1·04814	14·97038	22·07797

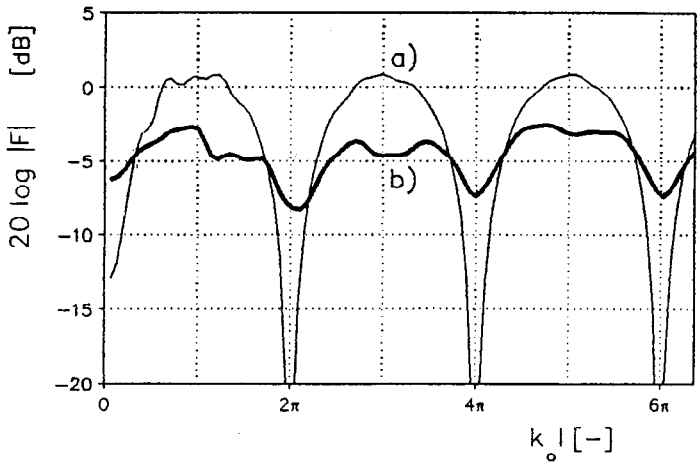

Fig. 14. Dependences of modul $|F|$ on kl for a) cylindric transducer ($a_1 = a_2 = 1{\cdot}5$ mm and $l = 1$ mm) b) conic transducer ($a_1 = 0{\cdot}5$ mm, $a_2 = 2{\cdot}4$ mm and $l = 1{\cdot}5$ mm).

On substituting the impedances from equations (15) to (17) into equations (12) and (13), we can calculate fraction F in equations (9) and (10). In the first approximation the velocity c in the conic part may be considered as velocity in a thin rod, c_0, which is independent of frequency. Fig. 14 shows the dependences of modul $|F|$ on kl, referring to both a cylindrical transducer ($a_1 = a_2 = 1{\cdot}5$ mm and $l = 1$ mm) and conic transducer ($a_1 = 0{\cdot}5$ mm, $a_2 = 2{\cdot}4$ mm and $l = 1{\cdot}5$ mm). For a cylindrical transducer the characteristic goes to zero at $kl = 2\pi$, 4π, etc., which was expected, while for a conic transducer at identical values kl there are minimums on the characteristic.

To simulate the behaviour of a real transducer as closely as possible, the velocities c_0 must be replaced by some more realistic entity. In the case of a cylindrical transducer we may use the well-known Puchhammer dispersion relation for phase velocity in cylindric rod in dependence on frequency. For a conic transducer there exists no exact correction. For our calculations we used the approximation of dispersion

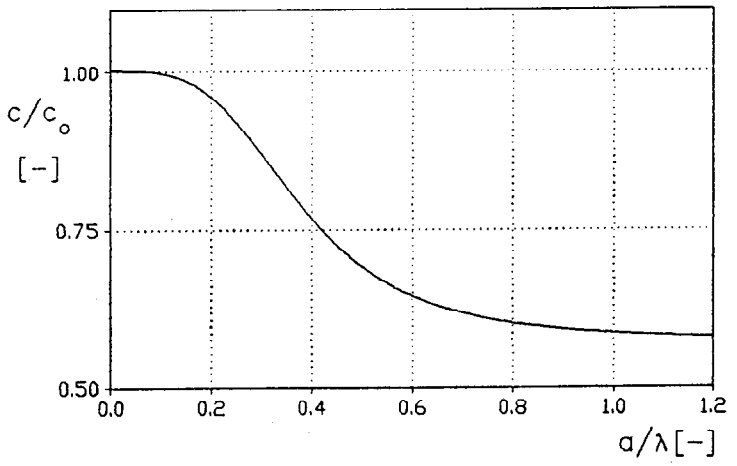

Fig. 15. Approximation of dispersion dependence of phase velocity on wave length by [3].

dependence (Fig. 15) presented in [3].

$$\frac{c}{c_0} \cong \frac{0{\cdot}0686\sigma^{1{\cdot}2162}}{\left(\frac{a}{\lambda}\right)\frac{1}{0{\cdot}144 + 0{\cdot}5017\sigma} + 0{\cdot}1443\sigma^{1{\cdot}1372}} + 0{\cdot}6124 - 0{\cdot}1432\sigma$$

where σ is Poisson's ratio, a is rod diameter, and λ is wave length.

Fig. 16 illustrates the dependence of modul $|F|$ on kl for a cylindrical transducer ($a_1 = a_2 = 1{\cdot}5$ mm and $l = 1$ mm), obtained

a) without using the exact Pochhammer solution for a cylindrical rod, and

b) using this solution.

Now we will discuss the influence of the material of the load- and source impedances. For a cylindrical transducer the material of the load impedance is as important as the material of the source, whereas for a conic transducer with, for instance, $r = a_2/a_1 = 5$ (the ratio of areas is 25) the load impedance Z_2 is relatively

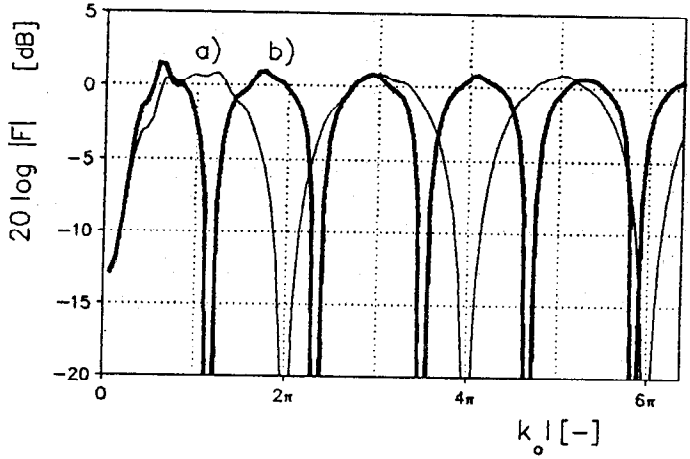

Fig. 16. Dependence of modul $|F|$ on kl for cylindrical transducer a) without correction b) with Pochhammer's velocity correction.

animportant. Fig. 17a shows the dependence of modul $|F|$ on kl of a cylindrical transducer for two various materials of the end block, while the material of the source remains in both the cases unchanged; Fig. 17b indicates the same situation for a conic transducer with $r = 5$. It is seen that the material of the end block of a cylindrical transducer playes an important role, whereas by using a conic transducer its role is unimportant. This is further advantage of conic transducer. Fig. 17c shows the characteristics of a conic transducer with the same brass end block but different materials of the source. As expected, the difference in characteristics confirms the necessity of calibrating on the respective material on which will be the transducer used.

5. MEASURING APPARATUS

The scheme of the apparatus for calibration of reference conic transducer for both the surface- and subsurface excitation is shown in Figs. 18a and 18b. The supporting arrangement is shown in Fig. 20.

The device for measuring the force aroused by breaking a glass capillary is situated below the block F. The knowledge of this force is necessary for absolute calibration of transducers. The device consists of a tensiometric bridge connected through a bonding agent with a duralumin intermediate element, further of a balance equipment and voltmeter. A detailed scheme of block F is shown in Fig. 19.

Two semicondutor tensiometers (T_2, T_4) are connected through a bonding agent with a thin rod of the intermediate element. This rod serves for breaking the glass

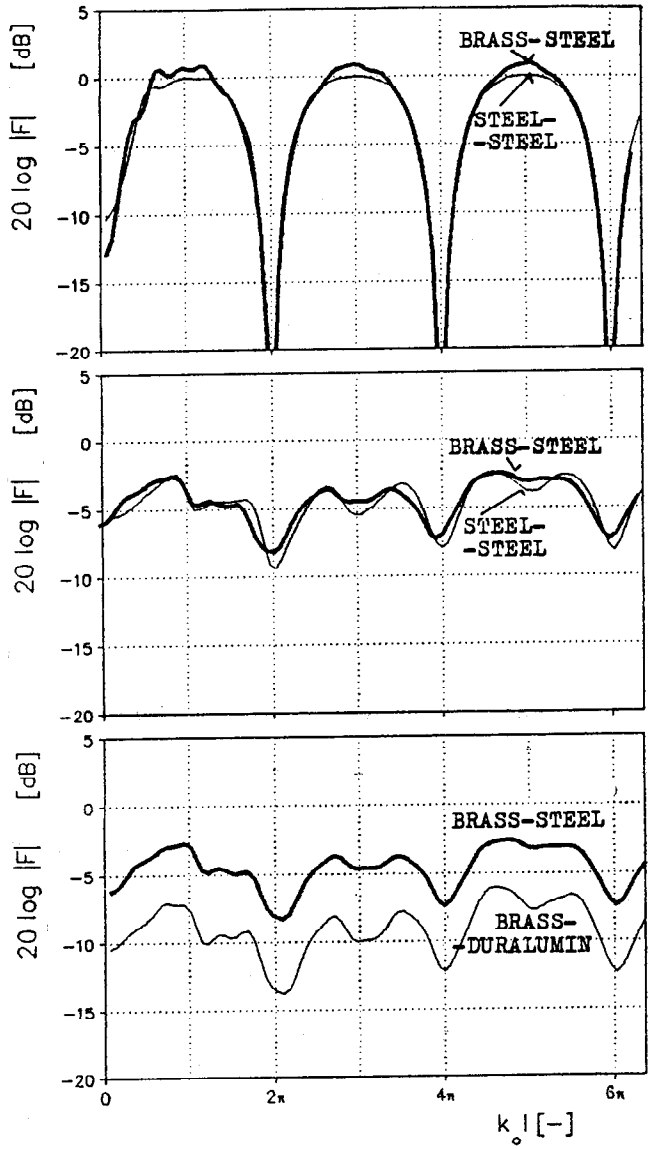

Fig. 17a. Dependence of modul $|F|$ on kl of cylindrical transducer for two various materials of the end block.

Fig. 17b. Dependence of modul $|F|$ on kl of a conic transducer ($r = 5$) for two various materials of the end block.

Fig. 17c. Dependence of modul $|F|$ on kl of a conic transducer ($r = 5$) for two various materials of the source and for an end block made of brass.

capillary. Two further semiconductor tensiometers (T_1, T_3) serving for temperature compensation are connected through a bonding agent with the enlarged part of the intermediate element.

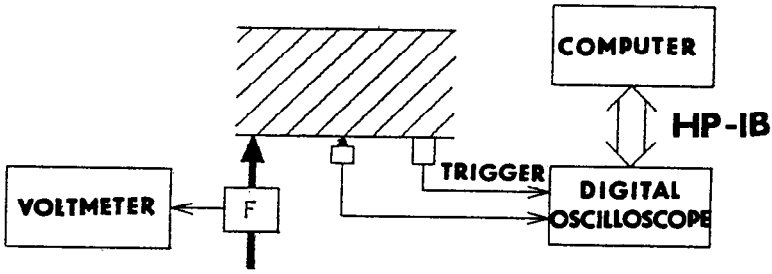

Fig. 18a. Scheme of the device for calibration of conic transducer by surface excitation.

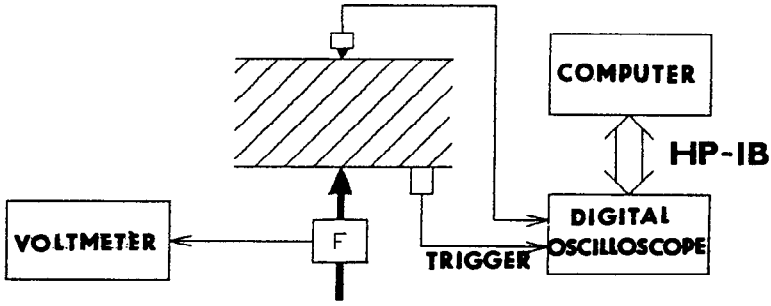

Fig. 18b. Scheme of the device for calibration of conic transducer by subsurface excitation.

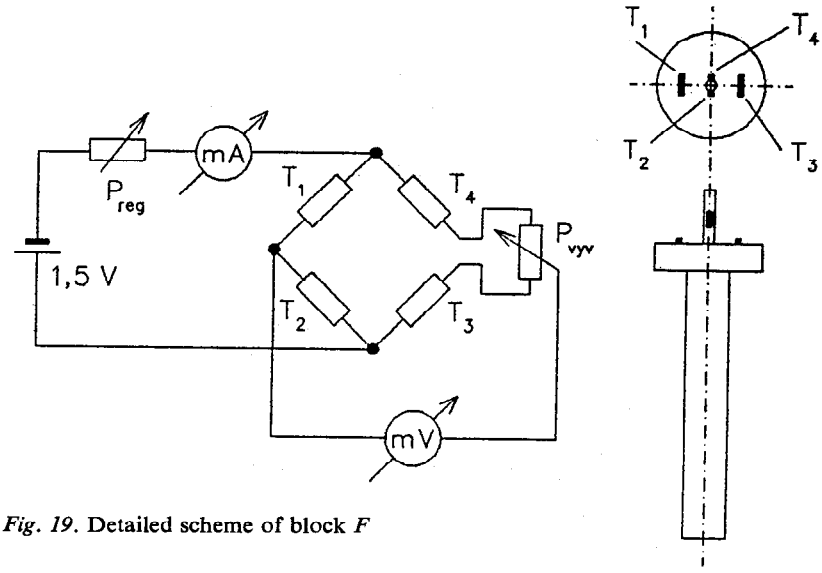

Fig. 19. Detailed scheme of block *F*

The bridge is supplied from 1·5 V source. The output voltage of the bridge, attaining units of mV, is measured by a KIESLEY voltmeter. Using rheostat R_r the current in tensiometric bridge is first adjusted to 5 mA, and the bridge is in no load operation balanced through potencipmeter P_v to zero. Then the bridge is calibrated by loading the device by forces whose magnitude is known. The calibration is repeated after finishing the measuring, to verify stability of parameters of the bridge.

The capillaries used for generating the exciting force in the form of a step function have principal importance for the function of calibrating device. We used capillaries made of silica glass, with outside diameter 100 μm and inside diameter 50 μm. It is to be remarked that capillaries with an outside diameter 1 mm, used in first experiments, proved to be unfitting, since the breaking process was not abrupt.

A steel block in the form of a cylinder with diameter 195 mm and height 140 mm has been used for callibration. The two bases of the steel cylinder were smoothed to a high gloss. The roughness of the surface was measured using a TAYLOR HOBSON apparatus in laboratories of the faculty of mechanical engineering ČVUT. The results of measuring are listed in Tab. 7 where S is the selective decisive deviation.

Table 7. Parameters of roughness of two bases of trial steel cylinder.

UPPER BASE				
	S	$\overline{X}$	X_{max}	X_{min}
R_a [ym]	0·004	0·086	0·090	0·083
LOWER BASE				
	S	$\overline{X}$	X_{max}	X_{min}
R_a [μm]	0·027	0·111	0·141	0·087

The cylinder was situated on three steel balls embeded in steel cylinders of the supporting device shown in Fig. 20.

The signal from a conic transducer enters a digital oscilloscope (KIKUSUI 7201A). The starting signal was taken from a classical resonant transducer of acoustic emission, sitauted in proximity of the exciting source. Both the signal from a conic transducer and starting signal were scaled by frequency 20 MHz, and stored in the memory of the oscilloscope. On storing several records, the records were carried over a digit transfer bus HP-IB into computer PC AT for further processing.

6. RESULTS OF CALIBRATION

The signal from a conic transducer composed of 1024 values (length of the record 51·2 μs with scaling step 0·05 μs) was processed in the following way:

a) selection of an interval of length 25·6 μs (512 samples), inside which is the record influenced through no rebounds from the walls of the block,

b) inside the above interval selection of only each other sample because the

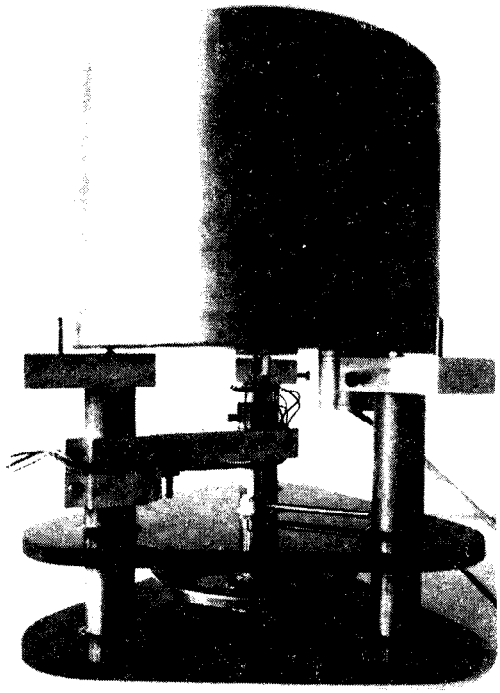

Fig. 20. Supporting device.

sampling step is unnecessarily small (high frequencies are considerably influenced through the noise, and we are interested in the range of frequency characteristic only up to 1 MHz); hence, the length of the record is 25·6 μs (256 samples),

c) calculation of a theoretical course of the displacement on the surface of the calibration block with equivalent time parameters,

d) execution FFT of signals obtained sub b) and c),

e) division of these spectra.

Figs 21, 22 and 23 show the results of calibration — frequency characteristics of a conic- and cylindrical transducer by calibrating through a surface- and subsurface excitation. The upper parts of the figures show the course of the signal, obtained by measurements, the middle parts indicate the theoretical course of displacement, and the lower parts illustrate the course of frequency characteristic of the used transducer, expressed in dB referred to V/μm.

Fig. 21 refers to calibration of a conic transducer with surface excitation.
Fig. 22 refers to calibration of a conic transducer with subsurface excitation.
Fig. 23 refers to calibration of a cylindrical transducer with subsurface excitation.

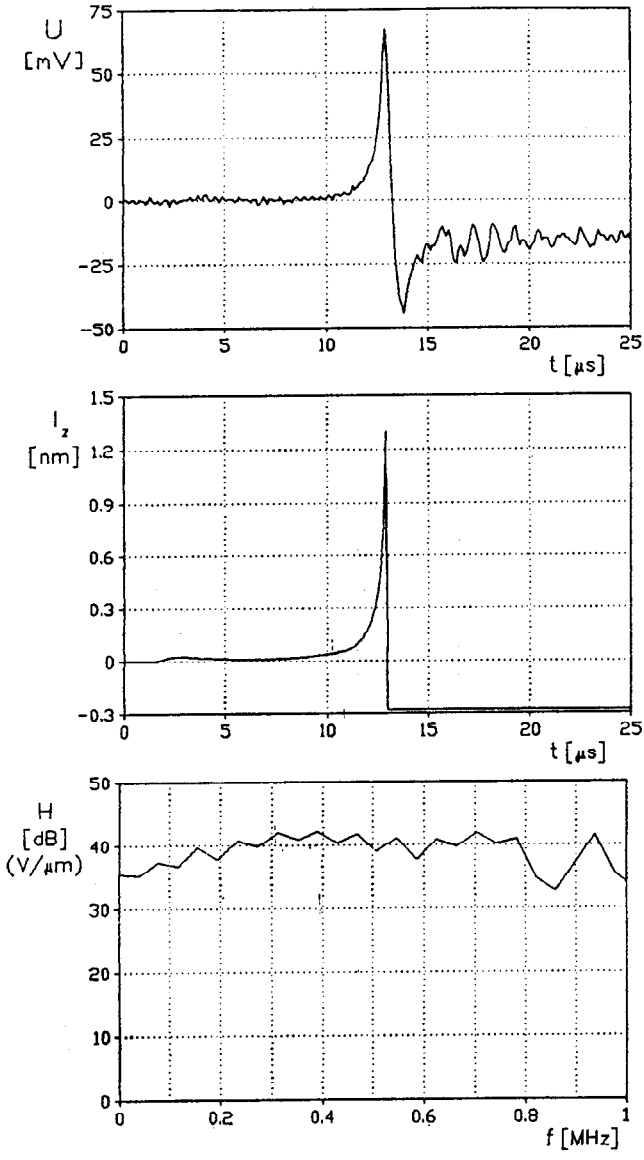

Fig. 21. Caracteristics of conic transducer by surface calibration.

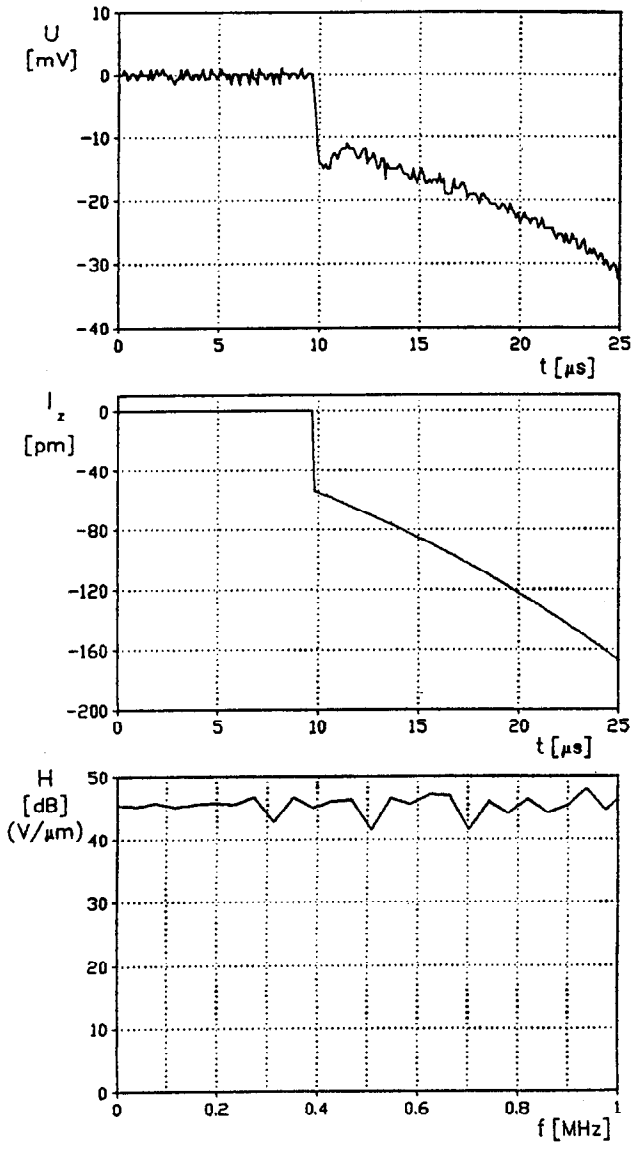

Fig. 22. Characteristics of conic transducer by subsurface calibration.

7. CONCLUSION

The paper presents results of numeric calculations of time dependences of a vertical component of displacement on the surface of a half-space by a surface- and subsurface excitation through a step function of force. We succeeded in determining explicit functions which can with sufficient accuracy approximate time dependences of a vertical

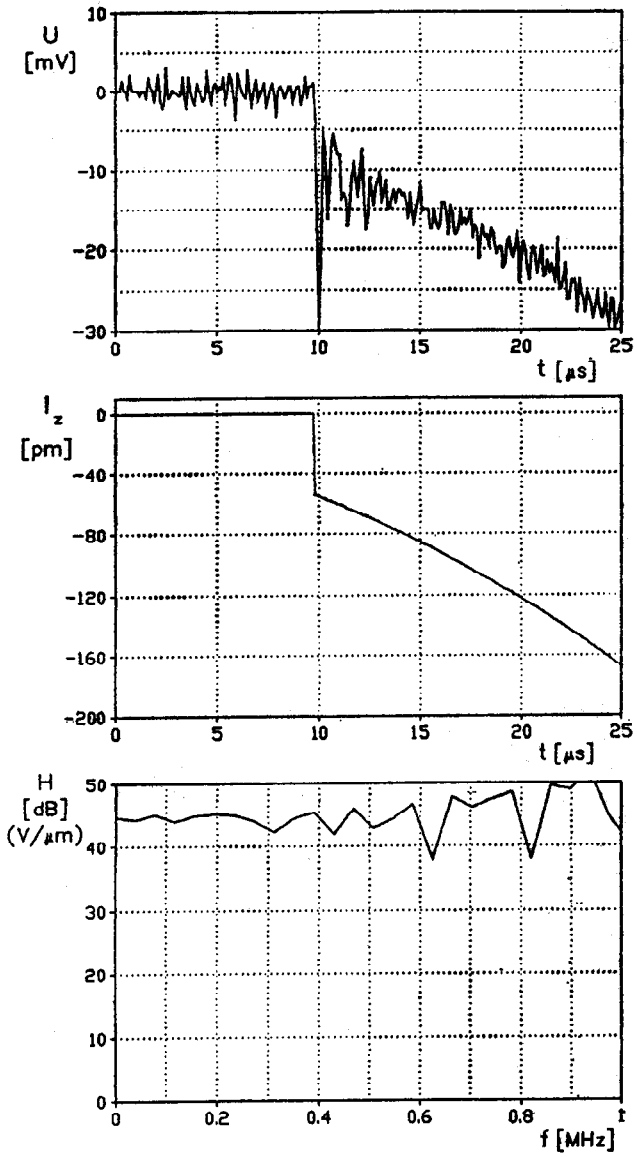

Fig. 23. Characteristics of cylindric transducer by subsurface calibration.

component of displacement on the surface of a half-space by a subsurface excitation. A maximum deviation of the approximating function from an exact course is for $r/h = 0$ only 0·86%. This accuracy is sufficient for practical calculations. The approximation allows the solution of complex integrals to be avoided, which brings considerable reduction of computation without decreasing the accuracy of solution.

Further, the paper presents analysis of a standard transducer of acoustic emission

(cylindrical transducer), and shows calibration of a conic- and cylindrical transducer. In frequency range from 0 to 1 MHz the two transducers have a uniform frequency characteristic with an average sensitivity 40 dB [V/μm].

The method described in the paper makes it possible to carry out an absolute calibration of transducers for acoustic emission, and thus it allows a quantitative comparison of transducers both imported and made in inland laboratories. The calibration of transducers is especially important for locating the sources of acoustic emission, where the knowledge of sensitivity of individual transducers is necessary.

Acknowledgement

The author wishes to thank doc. Ing. R. Brepta, DrSc. from ÚT-ČSAV in Prague for his valuable advice and help by accomplishing the paper. Acknowledgement is made also to ÚTSSK-ČSAV for affording a conic transducer for acoustic emission. I wish to express my gratidude also to Ing. L. Rufer, CSc. and to Mrs J. Remková for help by preparation and realization of measurements.

REFERENCES

[1] Cagniard, L.: Reflexion et réfraction des ondes séismiques progressives; Gauthiér-Villars, Paříž, 1939. [Reflection and refraction of progressive seismic waves; english translation Flynn, E. A. a Dix, C. H. McGraw-Hill, NewYork, 1962].

[2] Greenspan, M.: The NBS conical transducer: Analysis; J. Acoust. Soc. Am., Vol. 81, 1987, str. 173—183.

[3] Hégr, J.: Elektroakustická impulzní analýza soustav v pevně fázi; Kandidátská disertační práce ČVUT FEL, Praha, 1986.

[4] Hora, P.: Model zdroje akustické emise a vliv vazební vrstvy na snímaný signál akustické emise; Písemná práce k odborné kandidátské zkoušce, ČVUT FEL, Praha, 1989.

[5] Hora, P.: Kalibrace snímačů akustické emise impulsní metodou; Kandidátská disertační práce ČVUT FEL, Praha, 1990.

[6] Mohamed, A.: Equivalent circuits of solid horns undergoing longitudinal vibration; J. Acoust. Soc., Am. Vol. 38, 1965, str. 862—866.

[7] Mooney, H. M.: Some numerical solutions for Lamb's problem B. Seism. Soc. Am., Vol. 64, 1974, str. 473—491.

[8] Pekeris, C. L.: The seismic surface pulse; Proc. Natl. Acad. Sci., Vol. 41, 1955, str. 469.

[9] Pekeris, C. L.: The seismic buried pulse; Proc. Natl. Acad. Sci., Vol. 41, 1955, str. 629.

[10] Pekeris, C. L.; Lifson, H.: Motion of the surface of a uniform elastic half-space produced by a buried pulse; J. Acoust. Soc. Am., Vol. 29, 1957, str. 1233—1238.

[11] Škvor, Z.: Obvodové modely kmitajících soustav v pevné a plynné fázi; Studie ČSAV 16/86, Academia, Praha, 1986.

[Received November 12, 1990]

Ing. Petr Hora, Ústav technologie a spolehlivosti strojních konstrukcí ČSAV, Veleslavínova 11, 300 00 Plzeň, Czechoslovakia.